

# Hybrid Bilayer WSe<sub>2</sub>–CH<sub>3</sub>NH<sub>3</sub>PbI<sub>3</sub> Organolead Halide Perovskite as a High-Performance Photodetector

Junpeng Lu<sup>+</sup>, Alexandra Carvalho<sup>+</sup>, Hongwei Liu, Sharon Xiaodai Lim, Antonio H. Castro Neto,<sup>\*</sup> and Chornng Haur Sow<sup>\*</sup>

**Abstract:** A high-performance 2D photodetector based on a bilayer structure comprising a WSe<sub>2</sub> monolayer and CH<sub>3</sub>NH<sub>3</sub>PbI<sub>3</sub> organolead halide perovskite is reported. High performance is realized by modification of the WSe<sub>2</sub> monolayer with laser healing and perovskite functionalization. After modification, the output of the device was three orders of magnitude better than the pristine device; the performance is superior to that of most of the 2D photodetectors based on transition-metal-dichalcogenides (TMDs). This result indicates that combinatory TMDs–halide perovskite hybrids can be promising building blocks in optoelectronics.

Among TMDs, WSe<sub>2</sub> is promising because it possesses excellent optical properties in its monolayer form.<sup>[1–4]</sup> To date, the WSe<sub>2</sub> monolayer has been utilized in novel devices, such as electrically tunable excitonic LEDs,<sup>[4]</sup> gate controlled p–n junction diodes,<sup>[2]</sup> atomic monolayer solar cells,<sup>[3]</sup> and ambipolar field-effect transistors (FETs).<sup>[5,6]</sup> However, implementation of monolayer WSe<sub>2</sub> in wider applications is restricted by intrinsic constraints, such as chalcogen vacancies. These vacancies cause the device to exhibit comparatively low conductivity and photoconductivity.

Recently, we developed a laser-healing method that can significantly reduce unwanted carrier traps by passivating these vacancies with oxygen substitution. The photoconduction of the WSe<sub>2</sub> monolayer was significantly enhanced.<sup>[7]</sup> However, the critical parameters of a high-performance optoelectronic device are still restricted by the intrinsic nature of the TMDs monolayers. Interface engineering has been explored to overcome such intrinsic restrictions in the form of heterojunctions. Functionalization of 2D TMDs is achieved by the formation of interfaces with other attractive

materials. For example, interfacing with metal nanoparticles or organic dye molecules has been demonstrated as an effective strategy to control their optoelectrical properties.<sup>[8–10]</sup> Organolead halide perovskites have emerged as a new class of materials with high carrier mobility and lifetime, and large absorption coefficient, among other attributes. Additionally, a layer of the organolead halide perovskite can be easily added onto TMDs by low-cost processes, such as thermal evaporation. Herein, we introduce effective methods for enhancing the performance of a WSe<sub>2</sub> monolayer photodetector using a combination of laser healing and perovskite functionalization. By depositing a thin layer of organolead halide perovskite (CH<sub>3</sub>NH<sub>3</sub>PbI<sub>3</sub>) onto the laser healed WSe<sub>2</sub> monolayer by thermal evaporation, a high-performance TMD/perovskite 2D hybrid photodetector is attained. The combination of focused laser beam technique, which engineers and heals the defects in TMDs, and application of CH<sub>3</sub>NH<sub>3</sub>PbI<sub>3</sub>, which has a large absorption coefficient, facilitates formation of a superior photodetector with ultrahigh photoresponsivity and quantum efficiency. The optimized hybrid device is sensitive to a wide spectral range and exhibits more than three orders of magnitude higher output characteristics than a device based on pristine monolayer.

The fabrication of photodetectors involves WSe<sub>2</sub> monolayer flakes grown on transparent sapphire substrates by chemical vapor deposition.<sup>[7,11]</sup> An optical image in Figure S2a (Supporting Information) shows that most of the as-grown flakes are monolayers with triangular or star-like shapes. Atomic force microscopy (AFM) results confirm the monolayer thickness (ca. 0.7 nm; Supporting Information, Figure S2b). The device architecture of the hybrid photodetector is illustrated in Figure 1a. For photoresponsive studies, light illumination was applied to the device from either the top or bottom side. An optical image of a typical device is shown in Figure S2c (Supporting Information).

Figure 1b depicts the atomic structure of the hybrid perovskite/WSe<sub>2</sub> interface. Density functional theory (DFT) was used to provide further insight into the structure of the interface. Details of the commensurate interface model used, and the resulting misfit strain are given in the Supporting Information. It was found that the CH<sub>3</sub>NH<sub>3</sub>-terminated perovskite monolayer is stable, as suggested by Umari et al.,<sup>[12]</sup> while the PbI<sub>2</sub>-terminated monolayer departs considerably from the bulk structure. The dipoles on both sides are aligned approximately parallel with respect to the surface. The resulting contact potential difference between perovskite and WSe<sub>2</sub> was only 0.3 eV.

[\*] Dr. J. Lu,<sup>[+]</sup> Dr. S. X. Lim, Prof. A. H. Castro Neto, Prof. C. H. Sow  
Department of Physics, National University of Singapore  
2 Science Drive 3, Singapore 117542 (Singapore)  
E-mail: physowch@nus.edu.sg

Dr. J. Lu,<sup>[+]</sup> Dr. A. Carvalho,<sup>[+]</sup> Prof. A. H. Castro Neto, Prof. C. H. Sow  
Center for Advanced 2D Materials and Graphene Research Center,  
National University of Singapore  
6 Science Drive 2, Singapore 117546 (Singapore)  
E-mail: phycast@nus.edu.sg

Dr. H. Liu  
Institute of Materials Research and Engineering, A\*STAR (Agency for  
Science, Technology and Research)  
2 Fusionopolis Way, Innovis, #08-03, Singapore 138634 (Singapore)

[+] These authors contributed equally to this work.

Supporting information for this article, including experimental and calculation methods, can be found under:  
<http://dx.doi.org/10.1002/anie.201603557>.

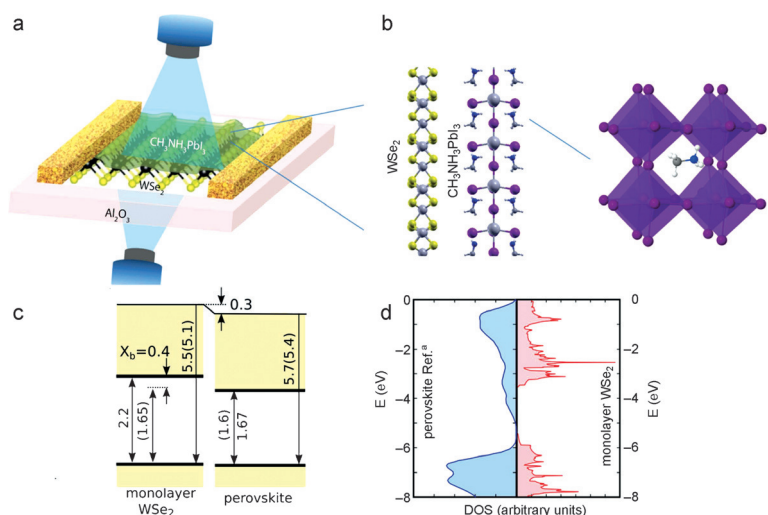


**Figure 1.** a) Device configuration schematic. b) Atomic structure of a model  $\text{CH}_3\text{NH}_3\text{PbI}_3/\text{WSe}_2$  monolayer interface and the perovskite structure. c) Heterojunction band structures using the data from Refs. [14, 17–20]. Theoretical values (brackets) are taken from Refs. [12, 14–16, 21–24] (Supporting Information, Table S1). All energies are in eV. d) Alignment of the densities of states of the perovskite/ $\text{WSe}_2$  (\*relativistic GW data from Ref. [12]) and relativistic DFT, corrected to the GW gap.<sup>[22]</sup>

This information was used to construct the energy band diagram for the device. In the real system,  $\text{WSe}_2$  is a monolayer but the perovskite is much thicker than the exciton radius, therefore it is approximated as bulk. The thickness does not affect the interface dipole directly, which is primarily determined by the orientation of  $\text{CH}_3\text{NH}_3$  at the interface, and to a lesser extent by the redistribution of the charge densities of the two moieties upon contact. Moreover, the perovskite band gap is almost independent of thickness.

According to the literature, the  $\text{WSe}_2$  monolayer and the bulk perovskite have almost the same optical band gap (1.65 and 1.6 eV, respectively)<sup>[13,14]</sup> and similar work functions (ca. 5.1 and 5.4 eV, respectively).<sup>[6,15,16]</sup> The actual band structure gap is larger by an amount corresponding to the exciton binding energy ( $X_b$ ; Figure 1c). However, in the combined system the screening by the perovskite likely reduces the exciton binding energy to a negligible value (justifying the lack of excitonic effects in the optical response of the device, as will be discussed later on).

The junction of the hybrid system is therefore expected to be type-II, that is a staggered gap. The band offsets, both at the valence band and conduction band, are very small. Excitons in either moieties can be spontaneously separated into a free hole in the  $\text{WSe}_2$  monolayer and a free electron in the perovskite.

Band gaps of both perovskite and the  $\text{WSe}_2$  monolayer were previously calculated by GW (Green's function (G) and the dynamically screened interaction (W)). Plotting the relativistic density of states of the  $\text{WSe}_2$  monolayer (corrected to the GW band gap using the procedure in ref. [22]) against the relativistic GW density of states of bulk  $\text{CH}_3\text{NH}_3\text{PbI}_3$  (Figure 1d), we find a qualitatively similar band offset to that found using the experimental data in Figure 1c. Additionally, we find alignment of the peaks of the high density of states close to the valence and conduction band edges of the  $\text{WSe}_2$  monolayer and  $\text{CH}_3\text{NH}_3\text{PbI}_3$ , which contributes to the efficient exciton dissociation.

To investigate the factors that enhance the performance of the photodetectors, we fabricated four different types of devices: pristine  $\text{WSe}_2$  monolayer ( $D_1$ ), pristine  $\text{WSe}_2$  monolayer with  $\text{CH}_3\text{NH}_3\text{PbI}_3$  ( $D_2$ ), laser annealed  $\text{WSe}_2$  monolayer ( $D_3$ ), and laser annealed  $\text{WSe}_2$  monolayer with  $\text{CH}_3\text{NH}_3\text{PbI}_3$  ( $D_4$ ). The output characteristics of these photodetectors were compared against each other. Figure 2 shows the performance of photodetector  $D_1$  and  $D_2$ . Typical I–V curves of  $D_1$

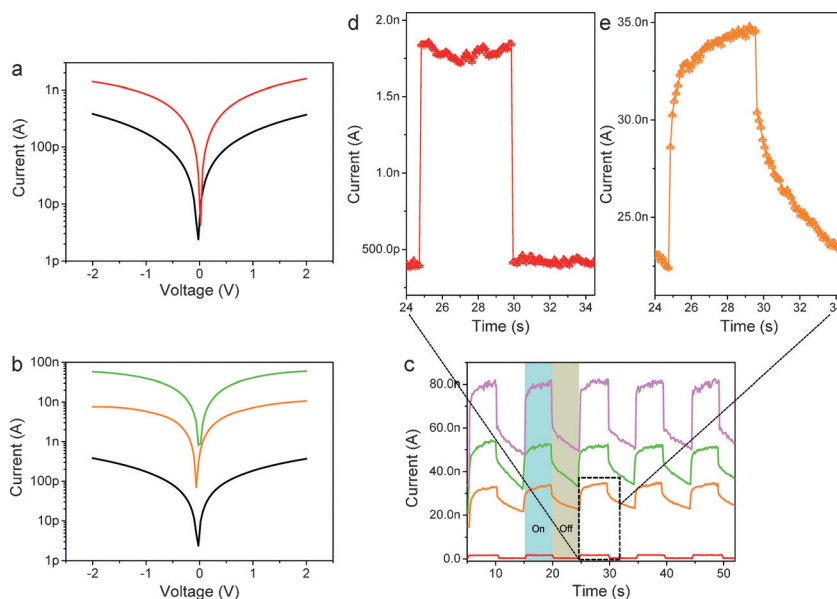


**Figure 2.** Output characteristics of a)  $D_1$  (dark (black), light (red)) and b)  $D_2$  (pristine dark (black), with perovskite in the dark (orange), with perovskite in the light (green)). c) Periodic photoresponse behavior of  $D_1$  and  $D_2$  (pristine  $V = 2$  V (red), perovskite  $V = 0.5$  V (orange), perovskite  $V = 1$  V (green), perovskite  $V = 2$  V (pink)). d) and e) Magnified view of the highlighted region of (c).

(Figure 2a) were measured in dark and illuminated conditions. The measurements were carried out under the irradiation of a diode laser ( $\lambda = 532$  nm, power = 2.8 mW) with light intensity that is insufficient to cause laser annealing of the  $\text{WSe}_2$ .<sup>[7]</sup> The output current exhibits a clear increase when the laser beam illuminates the device. However, the amplitudes of

the outputs for both devices are low. On the same grown substrate, we made another pristine device ( $D_1'$ ) similar to  $D_1$ ;  $D_1'$  and  $D_1$  perform similarly (Supporting Information, Figure S4). Under light illumination, the  $\text{WSe}_2$  monolayer absorbs photons and electron-hole pairs are created. Upon combined action of an applied voltage and the Schottky barrier, the generated electron-hole pairs are separated to form photocurrent. However, the inevitable chalcogen vacancies in the pristine  $\text{WSe}_2$  film trap the photocarriers, resulting in low photocurrent output.

To examine the effect of interface functionalization of perovskite, a thin layer of  $\text{CH}_3\text{NH}_3\text{PbI}_3$  (a few nanometers) was deposited onto  $D_1$  by thermal evaporation<sup>[25]</sup> to form the hybrid device,  $D_2$ . Figure 2b shows the I–V curves of  $D_2$  in the dark and under illumination conditions. The output current increases to approximately 10 nA at 2 V and this is about 30 times higher than  $D_1$ . The corresponding time response of the output of  $D_1$  and  $D_2$  (Figure 2c) was measured with periodic light illumination at a power density of  $70 \text{ mW cm}^{-2}$ . The current–time curve of  $D_1$  at 2 V (red curve) exhibits a rapid on and off behavior. Photoresponsivity ( $R_{\text{res}} = I_{\text{ph}}/P_{\text{eff}}$ ), where  $I_{\text{ph}}$  is the output photocurrent and  $P_{\text{eff}}$  is the effective optical power illuminated onto the working area, is one of the critical parameters of a photodetector.  $R_{\text{res}}$  of  $D_1$  is calculated to be about  $30 \text{ mA W}^{-1}$ . Accordingly, the external quantum efficiency,  $\text{EQE} = (hcR_{\text{res}})/(e\lambda)$ , is obtained as approximately 7.0%. These values place  $D_1$  in the medium range among the TMDs photodetectors.<sup>[2,26–28]</sup> Photodetectivity,  $D^* = (R_{\text{res}}S^{1/2})/(2eI_{\text{d}})^{1/2}$ , where  $S$  is the working area of the device and  $I_{\text{d}}$  is the dark current, is calculated to be about  $1.68 \times 10^9$  Jones. With periodic illumination,  $D_2$  also displays on and off behavior at different applied biases (0.5, 1, and 2 V; Figure 2c). The magnitude of the photocurrent at the same bias is much higher than that of  $D_1$ . The corresponding  $R_{\text{res}}$  and  $\text{EQE}$  were calculated to be  $1780 \text{ mA W}^{-1}$  and 415%, respectively; these values are about 60 times higher than those of  $D_1$ . Additionally, the photodetectivity for  $D_2$  was calculated to be approximately  $1.5 \times 10^{10}$  Jones. The temporal photoresponse changes from a simple fast transient process in  $D_1$  (Figure 2d) to a two-step process in  $D_2$  (Figure 2e), consisting of a fast–slow combination. The fast process of  $D_1$  and  $D_2$  is  $< 50 \text{ ms}$ , which is the detection limit of our equipment. The response time of the slower process of  $D_2$  can be extracted by fitting the rising curve using a biexponential function. The detailed analysis is shown in Figure S3 (Supporting Information). The slow process may be caused by carrier trapping and scattering at the interface.<sup>[29]</sup> Despite the improvement,  $D_2$  is only placed in the middle–upper range among TMDs photodetectors.<sup>[2,26–28]</sup> This is attributable to the chalcogen vacancies in pristine  $\text{WSe}_2$ . Recently, we developed an engineering strategy to passivate the vacancies. We made use of a focused laser beam to oxidize the pristine  $\text{WSe}_2$  film locally, after which the  $\text{WSe}_2$  film was found to exhibit improved conductivity.<sup>[7]</sup> By employing this method to treat  $D_1$ , which is another pristine device next to  $D_1$ , we fabricated the laser modified device  $D_3$ . The properties of  $D_3$  are shown in Figure 3a,c (green curves) and 3d. The comparison of  $D_1'$  and  $D_3$  is depicted in Figure S4 (Supporting Information). The output parameters  $R_{\text{res}}$ ,  $\text{EQE}$ , and  $D^*$  for  $D_3$  are calculated to

be  $4285 \text{ mA W}^{-1}$ , 999%, and  $1.7 \times 10^{10}$  Jones, respectively. All these values are higher than those of  $D_1$  and  $D_2$ . The enhancement is attributed to the oxygen passivation of the chalcogen vacancies in  $\text{WSe}_2$ .<sup>[7]</sup> To further modify the performance of the photodetectors,  $D_3$  was coated with a layer of perovskite to form a hybrid device,  $D_4$ . Typical I–V curves of the devices are shown in Figure 3b. The output current of  $D_4$  increased to sub-microamperes at 2 V. This is three orders higher than  $D_1$  and one order higher than  $D_3$ . Similarly, the photoresponse of  $D_4$  was measured by periodic illumination at different applied biases (Figure 3c) and it exhibits superior performance. The corresponding  $R_{\text{res}}$  and  $\text{EQE}$  for  $D_4$  are calculated to be approximately  $1.1 \times 10^5 \text{ mA W}^{-1}$  and 25000%, respectively. These values are more than 3000-fold higher than  $D_1$ , and much higher ( $10^5$  to  $10^6$  times) than earlier reports on TMDs monolayer/graphene phototransistors.<sup>[17,27]</sup> Accordingly,  $D^*$  of  $D_4$  is  $2.2 \times 10^{11}$  Jones which is more than two orders of magnitude higher than  $D_1$ . Additionally, the proportion of the slow process increases in the photoresponse process (Figure 3e). Detailed analysis of the slow process is shown in Figure S5 (Supporting Information). As summarized from the calculated parameters (Table 1), both the responsivity and sensitivity of the photodetector are enhanced by two to three orders of magnitude by the combined effect of laser healing and perovskite interfacing of the  $\text{WSe}_2$  monolayer.

**Table 1:** Summary of the performance of all devices and a comparison with previous reports.

	$R_{\text{res}}(\text{mA W}^{-1})$	$\text{EQE}(\%)$	$D^*(\text{Jones})$
$D_1/D_1'$	30/25	7.0/5.8	$1.68\text{E}9/1.5\text{E}9$
$D_2$	1780	415	$1.5\text{E}10$
$D_3$	4285	999	$1.7\text{E}10$
$D_4$	$1.1\text{E}5$	$2.5\text{E}4$	$2.2\text{E}11$
Graphene[Ref35]	0.5	6–16	NA
$\text{MoS}_2$ [Ref32]	0.42	NA	NA
$\text{WSe}_2$ [Ref8–10]	16	0.2–5	NA
$\text{MoS}_2/\text{dye}$ [Ref21]	1.38	NA	$3.5\text{E}5$

To gain further insight into the interface, DFT was utilized. The calculated DOS and band structure of the as-grown  $\text{WSe}_2$  monolayer containing Se vacancies ( $\text{V}_{\text{Se}}$ ) show deep gap levels arising from dangling bonds (Figure 4a). These deep gap levels (acceptors) are efficient traps for photogenerated electrons. Once negatively charged, they attract holes, acting as recombination centers. However, if the material is laser healed<sup>[7]</sup> oxygen atoms replace the missing Se atoms, with which they are isoelectronic, thereby removing the gap levels (Figure 4b). Since the laser healing gives rise to a  $\text{WSe}_2$  monolayer without defect states in the band gap, the spectral response of the devices would be different. The photoresponsivity of  $D_2$  and  $D_4$  versus wavelength is depicted in Figure 4c. Evidently,  $D_2$  exhibits a wider spectral response. This arises from the defect levels in the band gap of pristine  $\text{WSe}_2$ . The trap states provided by these levels also contribute to the photoresponse of the device.<sup>[19,20]</sup> The trap states have



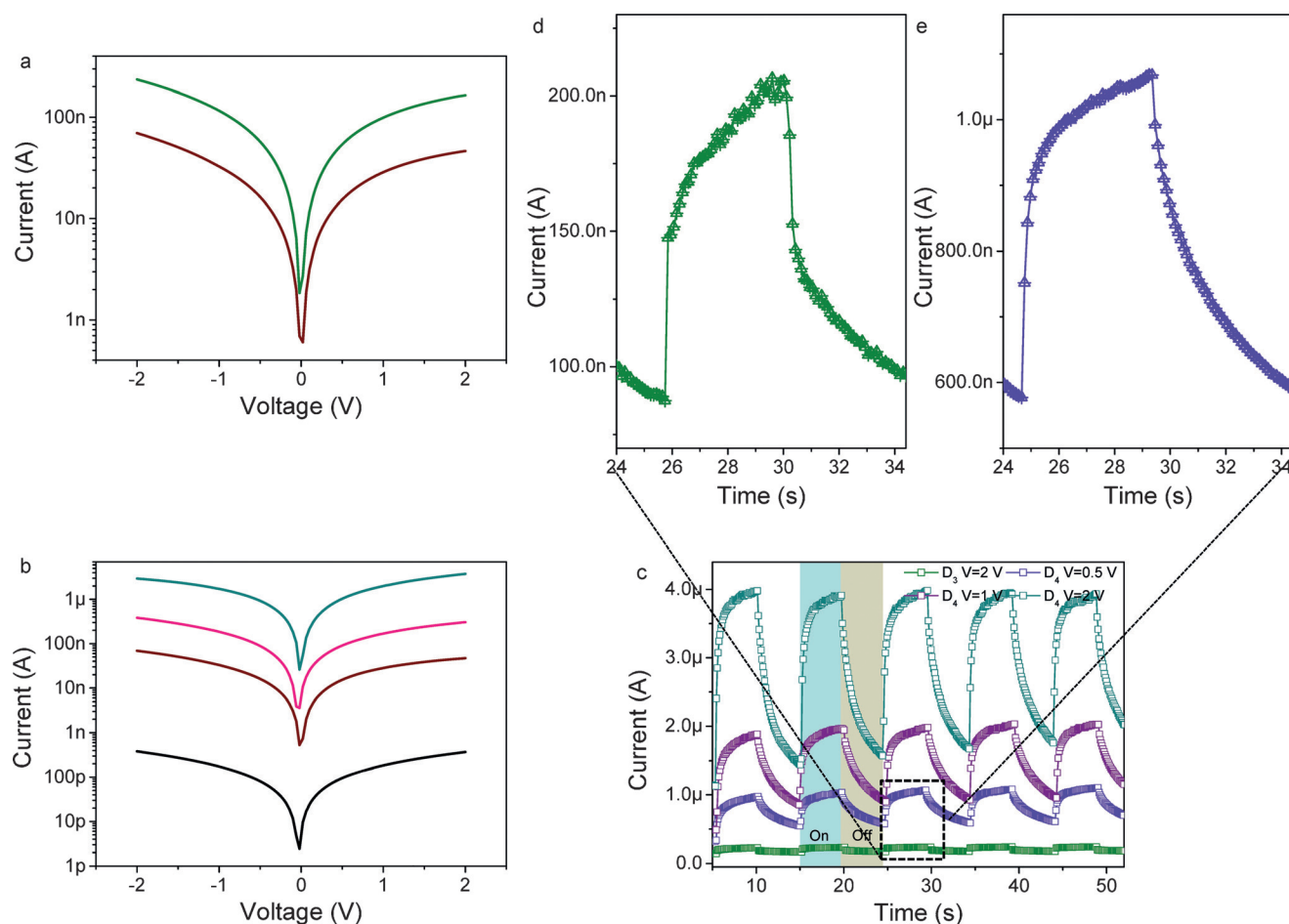


**Figure 3.** Output characteristics of a)  $D_3$  (dark (brown), light (green)) and b)  $D_4$  ( $D_1$  dark (black),  $D_3$  dark (brown),  $D_4$  dark (pink),  $D_4$  illuminated (cyan)). c) Periodic photoresponse behavior of  $D_3$  and  $D_4$ . d) and e) Magnified view of the highlighted region of (c).

their  $(-)/0$  transition level at  $E_c - 0.6$  eV. This facilitates the wider spectral response of  $D_2$  compared to  $D_4$ , where the response is restricted by the near perfect wide band gap of the laser-healed  $\text{WSe}_2$  monolayer. Figure 4d shows the micro UV/Vis absorption spectra collected from different material systems. The excitonic absorption peaks of the  $\text{WSe}_2$  monolayer are observed at about 760 nm (A exciton) and about 590 nm (B exciton). The large absorption in the higher energy region ( $< 500$  nm) is ascribed to the band nesting.<sup>[18]</sup> The spectrum of  $\text{CH}_3\text{NH}_3\text{PbI}_3$  shows its light harvesting capability, especially in the UV region. The small feature at approximately 748 nm results from the exciton transitions near the band edge.<sup>[30,31]</sup> After the construction of the heterostructure, the light harvesting capacity was significantly enhanced. Both excitonic absorption peaks of  $\text{WSe}_2$  disappeared but the band nesting absorption remained significant. After extracting the absorption signal contributed by  $\text{WSe}_2$ , the spectrum only exhibits band nesting features without the excitonic peaks. This suggests quenching of excitons. Photons absorbed in the band-nesting region would excite the electron-hole pairs that are more readily separated to form free carriers rather than excitons. This is because of the parallel nature of the conduction and valence bands in the band-nesting region (Supporting Information, Figure S6). Therefore, the separa-

tion of the photo-excited electron-hole pairs significantly raises the free carrier density, thereby increasing the output photocurrent.<sup>[32]</sup> Moreover, the distinct shift of the Raman features of the  $\text{WSe}_2$  monolayer, after coating with perovskite (Supporting Information, Figure S7) indicate the carrier doping of  $\text{WSe}_2$  from the formation of the heterojunction.<sup>[33]</sup>

In summary, we present a high-performance 2D photo-detector based on a hybrid bilayer of  $\text{WSe}_2$ - $\text{CH}_3\text{NH}_3\text{PbI}_3$ . Optimized performance was achieved using laser healing and perovskite coating. Focused laser healing was employed to passivate the vacancies in as-grown  $\text{WSe}_2$  monolayers. After further judicious interface design by coating the laser-annealed  $\text{WSe}_2$  monolayer with organolead halide perovskite, a superior photodetector with high photoresponsivity, quantum efficiency, and photosensitivity was obtained.

### Acknowledgements

We acknowledge support from NRF grant "Novel 2D materials with tailored properties: beyond graphene" (R-144-000-295-281) and MOE-ARF grant R-144-000-357-112.

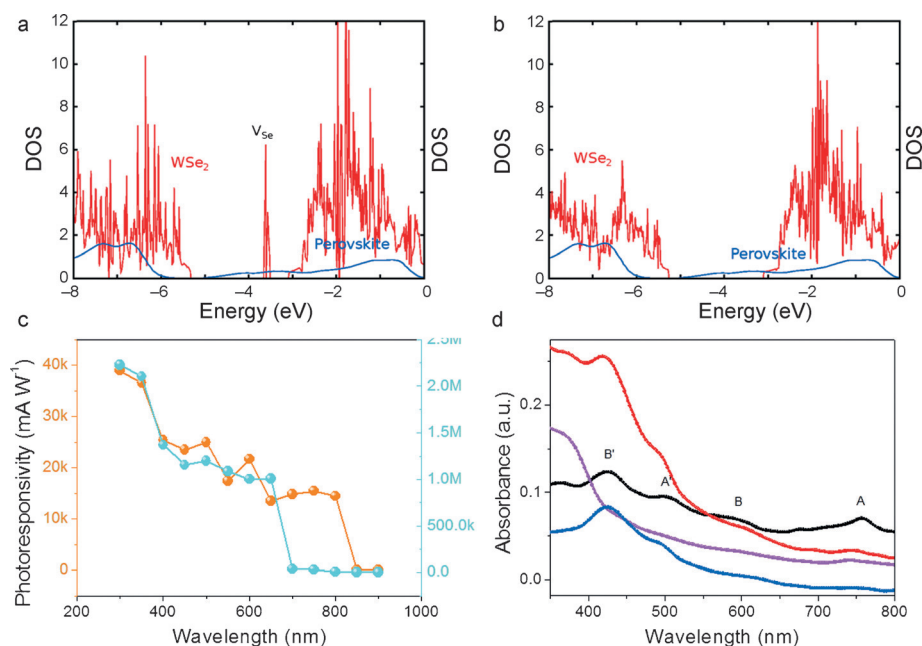


**Figure 4.** a) DOS of a monolayer of WSe<sub>2</sub> containing Se vacancies, aligned to the DOS of perovskite, taken from Ref. [12]. b) DOS of a monolayer of WSe<sub>2</sub>, where Se has been substituted by oxygen. For direct comparison, the DOS of the WSe<sub>2</sub> systems, obtained from relativistic DFT calculations, has been corrected to the GW gap following the mid-gap rule described in Ref. [22]. c) Photoresponsivity of D<sub>2</sub> and D<sub>4</sub> as a function of wavelength of incident light (pristine WSe<sub>2</sub> with perovskite (●), modified WSe<sub>2</sub> with perovskite (●)). d) UV/Vis spectra of WSe<sub>2</sub> monolayer (black), CH<sub>3</sub>NH<sub>3</sub>PbI<sub>3</sub> (purple), WSe<sub>2</sub> monolayer/CH<sub>3</sub>NH<sub>3</sub>PbI<sub>3</sub> heterostructure (red), and extracted spectrum of WSe<sub>2</sub> from the heterostructure (blue).

**Keywords:** 2D transition-metal-dichalcogenides · laser healing · optoelectronic devices · perovskite

**How to cite:** *Angew. Chem. Int. Ed.* **2016**, 55, 11945–11949  
*Angew. Chem.* **2016**, 128, 12124–12128

- [1] A. M. Jones, H. Yu, N. J. Ghimire, S. Wu, G. Aivazian, J. S. Ross, B. Zhao, J. Yan, D. G. Mandrus, D. Xiao, W. Yao, X. Xu, *Nat. Nanotechnol.* **2013**, 8, 634–638.
- [2] B. W. H. Baugher, H. O. H. Churchill, Y. Yang, P. Jarillo-Herrero, *Nat. Nanotechnol.* **2014**, 9, 262–267.
- [3] A. Pospischil, M. M. Furchi, T. Mueller, *Nat. Nanotechnol.* **2014**, 9, 257–261.
- [4] J. S. Ross, P. Klement, A. M. Jones, N. J. Ghimire, J. Yan, D. G. Mandrus, T. Taniguchi, K. Watanabe, K. Kitamura, W. Yao, D. H. Cobden, X. Xu, *Nat. Nanotechnol.* **2014**, 9, 268–272.
- [5] H. Fang, S. Chuang, T. C. Chang, K. Takei, T. Takahashi, A. Javey, *Nano Lett.* **2012**, 12, 3788–3792.
- [6] W. Liu, J. Kang, D. Sarkar, Y. Khatami, D. Jena, K. Banerjee, *Nano Lett.* **2013**, 13, 1983–1990.
- [7] J. Lu, A. Carvalho, X. K. Chan, H. Liu, B. Liu, E. S. Tok, K. P. Loh, A. H. Castro Neto, C. H. Sow, *Nano Lett.* **2015**, 15, 3524–3532.
- [8] T. S. Sreepasad, P. Nguyen, N. Kim, V. Berry, *Nano Lett.* **2013**, 13, 4434–4441.
- [9] S. H. Yu, Y. Lee, S. K. Jang, J. Kang, J. Jeon, C. Lee, J. Y. Lee, H. Kim, E. Hwang, S. Lee, J. H. Cho, *ACS Nano* **2014**, 8, 8285–8291.
- [10] J. Lu, J. H. Lu, H. Liu, B. Liu, L. Gong, E. S. Tok, K. P. Loh, C. H. Sow, *Small* **2015**, 11, 1792–1800.
- [11] J.-K. Huang, J. Pu, C.-L. Hsu, M.-H. Chiu, Z.-Y. Juang, Y.-H. Chang, W.-H. Chang, Y. Iwasa, T. Takenobu, L.-J. Li, *ACS Nano* **2014**, 8, 923–930.
- [12] P. Umari, E. Mosconi, F. De Angelis, *Sci. Rep.* **2014**, 4, 4467.
- [13] H. Sahin, S. Tongay, S. Horzum, W. Fan, J. Zhou, J. Li, J. Wu, F. M. Peeters, *Phys. Rev. B* **2013**, 87, 165409.
- [14] T. Dittrich, C. Awino, P. Prajontat, B. Rech, M. C. Lux-Steiner, *J. Phys. Chem. C* **2015**, 119, 23968–23792.
- [15] N. R. Pradhan, D. Rhodes, S. Memaran, J. M. Poumirol, D. Smirnov, S. Talapatra, S. Feng, N. Perea-Lopez, A. L. Elias, M. Terrones, P. M. Ajayan, L. Balicas, *Sci. Rep.* **2015**, 5, 8979.
- [16] P. Schulz, E. Edri, S. Kirmayer, G. Hodes, D. Cahen, A. Kahn, *Energy Environ. Sci.* **2014**, 7, 1377–1381.
- [17] F. Xia, T. Mueller, Y.-m. Lin, A. Valdes-Garcia, P. Avouris, *Nat. Nanotechnol.* **2009**, 4, 839–843.
- [18] A. Carvalho, R. M. Ribeiro, A. H. Castro Neto, *Phys. Rev. B* **2013**, 88, 115205.
- [19] B. Miller, E. Parzinger, A. Vernickel, A. W. Holleitner, U. Wurstbauer, *Appl. Phys. Lett.* **2015**, 106, 122103.
- [20] J. Y. Hou, S. J. Fonash, *Appl. Phys. Lett.* **1992**, 61, 186–188.
- [21] K. He, N. Kumar, L. Zhao, Z. Wang, K. F. Mak, H. Zhao, J. Shan, *Phys. Rev. Lett.* **2014**, 113, 026803.
- [22] Y. Liang, S. Huang, R. Soklaski, L. Yang, *Appl. Phys. Lett.* **2013**, 103, 042106.
- [23] T. C. Berkelbach, M. S. Hybertsen, D. R. Reichman, *Phys. Rev. B* **2013**, 88, 045318.
- [24] F. Brivio, K. T. Butler, A. Walsh, M. van Schilfgaarde, *Phys. Rev. B* **2014**, 89, 155204.
- [25] M. Liu, M. B. Johnston, H. J. Snaith, *Nature* **2013**, 501, 395–398.
- [26] W. Zhang, J.-K. Huang, C.-H. Chen, Y.-H. Chang, Y.-J. Cheng, L.-J. Li, *Adv. Mater.* **2013**, 25, 3456–3461.
- [27] Z. Yin, H. Li, H. Li, L. Jiang, Y. Shi, Y. Sun, G. Lu, Q. Zhang, X. Chen, H. Zhang, *ACS Nano* **2012**, 6, 74–80.
- [28] O. Lopez-Sanchez, D. Lembke, M. Kayci, A. Radenovic, A. Kis, *Nat. Nanotechnol.* **2013**, 8, 497–501.
- [29] P. Stokes, L. Liu, J. Zou, L. Zhai, Q. Huo, S. I. Khondaker, *Appl. Phys. Lett.* **2009**, 94, 042110.
- [30] M. M. Lee, J. Teuscher, T. Miyasaka, T. N. Murakami, H. J. Snaith, *Science* **2012**, 338, 643–647.
- [31] Y. Lee, J. Kwon, E. Hwang, C.-H. Ra, W. J. Yoo, J.-H. Ahn, J. H. Park, J. H. Cho, *Adv. Mater.* **2015**, 27, 41–46.
- [32] D. Kozawa, R. Kumar, A. Carvalho, K. Kumar Amara, W. Zhao, S. Wang, M. Toh, R. M. Ribeiro, A. H. Castro Neto, K. Matsuda, G. Eda, *Nat. Commun.* **2014**, 5.
- [33] B. Chakraborty, A. Bera, D. V. S. Muthu, S. Bhowmick, U. V. Waghmare, A. K. Sood, *Phys. Rev. B* **2012**, 85, 161403.

Received: April 14, 2016  
 Revised: June 26, 2016